hydrogen

MDPI

Article

Facile Engineering of Pt-Rh Nanoparticles over Carbon for Composition-Dependent Activity and Durability Toward Glycerol Electrooxidation

Marta Venancia França Rodrigues [1], Wemerson Daniel Correia dos Santos [1], Fellipe dos Santos Pereira [2], Augusto César Azevedo Silva [3], Liying Liu [4], Mikele Candida Sant'Anna [5], Eliane D'Elia [2], Roberto Batista de Lima [1,*] and Marco Aurélio Suller Garcia [6,*]

[1] Department of Chemistry, Federal University of Maranhao, Avenida dos Portugueses, 1966, São Luís 65080-805, MA, Brazil; marthafranca01@gmail.com (M.V.F.R.); wdcs1993@gmail.com (W.D.C.d.S.)
[2] Instituto de Química, Universidade Federal do Rio de Janeiro (UFRJ), Rio de Janeiro 21941-909, RJ, Brazil; fellipe.santos@pos.iq.ufrj.br (F.d.S.P.); eliane@iq.ufrj.br (E.D.)
[3] Departamento de Química (DQM)—Centro de Ciências da Educação e Naturais (CECEN), Universidade Estadual do Maranhão (UEMA), Maranhão 65055-310, MA, Brazil; augustosilva@professor.uema.br
[4] Centro Brasileiro de Pesquisas Físicas, Rio de Janeiro 22290-180, RJ, Brazil; lyliu.xing@gmail.com
[5] Curso de Engenharia Aeroespacial, Universidade Federal do Maranhão, São Luís 65080-805, MA, Brazil; mikele.candida@ufma.br
[6] Nanotechnology Engineering Program, Alberto Luiz Coimbra Institute for Graduate Studies and Research in Engineering (COPPE), Federal University of Rio de Janeiro, Avenida Horácio Macedo, 2030, Rio de Janeiro 21941-972, RJ, Brazil
* Correspondence: rb.lima@ufma.br (R.B.d.L.); marcosuller@pent.coppe.ufrj.br (M.A.S.G.)

Abstract

In this study, we report the synthesis, characterization, and performance evaluation of a series of bimetallic Pt_xRh_y/C electrocatalysts with systematically varied Rh content for glycerol electrooxidation in acidic and alkaline media. The catalysts were prepared via a polyol reduction method using ethylene glycol as both a solvent and reducing agent, with prior functionalization of Vulcan XC-72 carbon to enhance nanoparticles (NPs) dispersion. High-resolution transmission electron microscopy (HRTEM), energy-dispersive X-ray spectroscopy (EDS), and X-ray diffraction (XRD) analyses indicated the spatial co-location of Rh atoms alongside Pt atoms. Electrochemical studies revealed strong composition-dependent behavior, with $Pt_{95}Rh_5/C$ exhibiting the highest activity toward glycerol oxidation. To elucidate the origin of raised results, density functional tight binding (DFTB) simulations were conducted to model atomic distributions and evaluate energetic parameters. The results showed that Rh atoms preferentially segregate to the surface at higher concentrations due to their lower surface energy, while at low concentrations, they remain confined within the Pt lattice. Among the series, $Pt_{95}Rh_5/C$ exhibited a distinctively higher excess energy and less favorable binding energy, rationalizing its lower thermodynamic stability. These findings reveal a clear trade-off between catalytic activity and structural durability, highlighting the critical role of the composition and nanoscale architecture in optimizing Pt-based electrocatalysts for alcohol oxidation reactions.

Keywords: PtRh nanoparticles; glycerol electrooxidation; DFTB; stability

check for updates

Academic Editor: Aleksey A. Vedyagin

Received: 5 August 2025
Revised: 19 September 2025
Accepted: 1 October 2025
Published: 3 October 2025

Citation: Rodrigues, M.V.F.; Santos, W.D.C.d.; Pereira, F.d.S.; Silva, A.C.A.; Liu, L.; Sant'Anna, M.C.; D'Elia, E.; Lima, R.B.d.; Garcia, M.A.S. Facile Engineering of Pt-Rh Nanoparticles over Carbon for Composition-Dependent Activity and Durability Toward Glycerol Electrooxidation. *Hydrogen* **2025**, *6*, 78. https://doi.org/10.3390/hydrogen6040078

1. Introduction

The electrooxidation of polyols has attracted increasing attention as a promising pathway for energy conversion and the valorization of biomass-derived molecules in

low-temperature fuel cells [1,2]. Such an approach aligns with ongoing efforts to develop environmentally sustainable energy processes, employing nanostructured systems to enhance accessibility and address cost-related challenges [3–6]. Among these polyols, glycerol stands out due to its low cost, high hydrogen content, and the fact that it is a major byproduct of biodiesel production, representing an abundant and renewable feedstock. Generally speaking, the glycerol electrooxidation proceeds through adsorption on the catalyst, stepwise removal of hydrogen, formation of surface intermediates, and their oxidation assisted by OH species, ultimately yielding either partially oxidized products or complete oxidation to CO_2. In alkaline medium, the higher availability of OH^- ions facilitates the oxidation of poisoning intermediates (e.g., *CO), improves catalyst tolerance, and often results in higher activity and stability compared to acidic conditions [7]. Within this scenario, while several research groups are focused on developing selective pathways for alcohol electrooxidation [8,9], others have directed their efforts toward understanding how electrocatalysts could present enhanced resistance to CO poisoning and surface passivation by reaction intermediates [10,11].

Platinum (Pt)-based materials have long been regarded as benchmark electrocatalysts for alcohol oxidation reactions (AOR) owing to their superior intrinsic activity and electrical conductivity. Nevertheless, the catalytic performance of pure Pt is hindered by the strong binding of reaction intermediates and limited resistance to poisoning, which compromises both activity and long-term durability [12]. To overcome these limitations, mixing Pt with a second metal has emerged as an effective strategy to modulate its electronic structure and surface chemistry [13–15]. In particular, bimetallic Pt-based catalysts have demonstrated improved catalytic properties through synergistic and bifunctional mechanisms, including modified d-band center alignment and enhanced generation of surface hydroxyl groups for oxidative removal of adsorbed species [15].

Among potential metals, rhodium (Rh) offers a compelling combination of properties, also observed in several (electro)catalytic processes [16–19]. Rh exhibits a smaller atomic radius and lower surface energy compared to Pt, which affects atomic distribution and favors surface segregation under certain conditions [20,21]. More importantly, Rh is known for its oxophilic nature, enabling it to activate water molecules and form surface hydroxides at lower potentials. This property is especially beneficial for the oxidation of polyols, as it facilitates the cleavage of C–C bonds [22]. Additionally, this process could be performed via a bifunctional pathway where Rh provides oxidative species and Pt acts as the primary site for substrate adsorption and initial dehydrogenation [23,24]. PtRu/C is a well-established catalyst in alcohol electrooxidation, particularly valued for its high CO tolerance and ability to promote C–C bond cleavage. Several studies show that PtRu/C achieves lower onset potentials and higher current densities in glycerol oxidation than Pt/C alone [25]. For example, Kim et al. showed that a Pt_5Ru_5/C catalyst had an onset potential of ~0.448 V vs. RHE for glycerol oxidation (0.5 M H_2SO_4) compared to ~0.635 V vs. RHE for Pt/C, as well as superior stability and product distribution toward both C_3- and smaller oxidation products [26]. Thus, the literature lacks exploration of PtRh nanomaterials. And, despite these promising attributes, understanding how varying Pt:Rh ratios influence the balance between catalytic activity and durability remains limited. In this context, the rational design of PtRh bimetallic nanostructures requires a comprehensive analysis of how composition and energetics interplay to define performance under electrochemical conditions.

Therefore, in this work, we report the synthesis, characterization, and electrochemical evaluation of a series of Pt_xRh_y NPs (with different Pt:Rh ratios) supported on functionalized carbon (Pt_xRh_y/C) with systematically varied Rh content (5 to 20 at.%), prepared via a polyol route. An experimental strategy was employed to assess the morphology and spatial distribution of the metals of the support, while electrochemical measurements

probe catalytic activity and durability in glycerol oxidation. Additionally, density functional tight-binding (DFTB) simulations provide atomic-level insight into stability, surface segregation, and binding energetics. Our results reveal a composition-dependent trade-off, with $Pt_{95}Rh_5$/C displaying the highest activity, while $Pt_{90}Rh_{10}$/C demonstrates superior long-term stability. These findings highlight the critical role of metals' composition and surface arrangement in guiding the design of bimetallic electrocatalysts for sustainable energy applications.

2. Materials and Methods

2.1. Materials and Reagents

Most of the reagents used here were of analytical grade, acquired from Sigma-Aldrich (St. Louis, MO, USA), and utilized without additional purification. Carbon Black Vulcan XC-72 was sourced from Cabot Corporation (Boston, MA, USA). Commercial Pt/C 20 wt.% was purchased from Johnson Matthey Fuel Cells (Wiltshire, UK). Deionized water with a resistivity of 18.2 MΩ cm^{-1} (Millipore®, Burlington, MA, USA) was used to prepare all solutions. Transmission electron microscopy (TEM) and high-resolution TEM (HRTEM) analyses were performed using a JEOL JEM-2100F microscope (JEOL Ltd., Tokyo, Japan) operating at an accelerating voltage of 200 kV. For enhanced imaging resolution and elemental distribution analysis, additional HRTEM and energy-dispersive X-ray spectroscopy (EDS) mapping were conducted using a Talos F200X G2 microscope (Thermo Fisher Scientific, Waltham, MA, USA), equipped with a high-sensitivity EDS detector. X-ray diffraction (XRD) patterns were acquired on a D8 Discover diffractometer (Bruker Corporation, MA, USA) utilizing Cu Kα radiation (λ = 1.5406 Å), operated at 40 kV and 40 mA. A nickel filter was applied to suppress the Cu Kβ component, and a LynxEye position-sensitive detector enabled high-resolution data collection. Scans were conducted over a 2θ range of 10–100°, with a step size of 0.5° and a counting time of 5 s per step. The metal loading on the carbon support was determined by inductively coupled plasma optical emission spectrometry (ICP-OES) using an Arcos spectrometer (SPECTRO Analytical Instruments, Kleve, Germany).

2.2. Synthesis of Pt_xRh_y/C NPs

The NPs synthesis followed a previously reported method with modifications [13]. Four different compositions of Pt_xRh_y NPs were prepared, aiming to increase Rh content (with a total mass of metal of 20 wt.%). s an illustration, the synthesis of Pt:Rh (80:20) is detailed: 1.00 g of Vulcan XC-72 (pretreated with 5 mol·L^{-1} HNO_3 in an ultrasonic bath for 30 min) was added to a volumetric flask containing a solution of 424.9 mg of $H_2PtCl_6 \cdot 6H_2O$ and 102.3 mg of $RhCl_3 \cdot 3H_2O$ dissolved in 50 mL of ethylene glycol (EG). This suspension was stirred under reflux at 80 °C for 2 h to promote metal reduction and nanoparticle deposition onto the carbon support. After completion, the resulting material was cooled to room temperature, thoroughly washed with deionized water and ethanol, and dried in an oven at 60 °C for 2 h.

2.3. Electrochemical Measurements

The electrochemical measurements were conducted using Autolab PGSTAT 302 N equipment (Metrohm, Herisau, Switzerland) coupled to a computer with the NOVA 2.0 software. A three-electrode cell was utilized, where the glassy carbon electrode (GCE—3 mm) was used as the working electrode, and a saturated calomel electrode (SCE) and a platinum foil were used as the reference and counter electrodes, respectively. Before performing the electrochemical measurements, the GCE was modified with a previously prepared catalytic ink. For this, 2.5 mg of each catalyst was dispersed in 725 µL of deionized

water, 520 μL of methanol, and 30 μL of Nafion. The resulting suspension was placed in an ultrasonic bath for 1 h to ensure thorough homogenization. Afterwards, 5 μL of this suspension was drop-cast onto the surface of the GCE. The electrocatalysts were subjected to cyclic voltammetry (CV) in a saturated solution of N_2 with $HClO_4$ 0.5 M and KOH 0.1 M for 20 cycles before the addition of glycerol to the electrolyte, in the potential range of 0 to 1.6 V vs. RHE (acidic) and 0.09 to 1.7 V vs. RHE (alkaline) with a sweep speed of 50 $mV.s^{-1}$. Glycerol electrooxidation studies were carried out in 5–30 mM solutions under acidic conditions, and in 5–30 μM solutions under basic conditions. In the CO stripping experiment, the catalysts were subjected to CO adsorption for 10 min, and then the removal of CO gas dissolved in the electrolyte via N_2 purging for 20 min. CO stripping voltammetry was performed in the potential range of 0.05–0.9 V vs. RHE at a sweep rate of 50 mV/s. In this article, current densities were normalized by electrochemical surface areas (ECSA) measured via CO stripping, except for special instructions. The ECSA is calculated by:

$$ECSA = \frac{Q_{CO}}{0.42 \mu m/cm^2} \quad (1)$$

2.4. Density Functional Tight-Binding (DFTB) Methodology

The construction of the Pt_xRh_y NPs was performed using the OpenMD software (version 3.0) utility. This approach involves expanding the fractional coordinates of Pt atoms to generate a nanoparticle with spherical geometry. Subsequently, Rh atoms were randomly introduced into the structure following the experimental compositions, replacing Pt atoms to yield a bimetallic system. Following the structural construction, the resulting Pt_xRh_y NPs were subjected to geometry optimization at the DFTB level using the GFN1-xTB Hamiltonian, as implemented in the xTB methodology and code [27,28]. To assess the stability of the systems, two key energetic descriptors were calculated.

Binding Energy (E_b):

$$E_b = E(Pt_mRh_n) - mE_{atom}(Pt) - nE_{atom}(Rh) \quad (2)$$

Excess Energy (E_{exc}):

$$E_{exc} = E(Pt_mRh_n) - \frac{mE(Pt_N)}{N} - \frac{nE(Rh_N)}{N} \quad (3)$$

where N is the total number of atoms in the monometallic Pt and Rh reference NPs (here, 201 atoms), m and n are the numbers of Pt and Rh atoms in the cluster, respectively, and $E(Pt_mRh_n)$ is the total energy of the bimetallic nanostructure.

3. Results and Discussion

We started our investigation by synthesizing a series of bimetallic electrocatalysts using the polyol method, in which EG acts both as a solvent and a mild reducing agent. Importantly, we have introduced oxygen-containing functional groups onto the Vulcan XC-72 carbon black surface before the metal deposition, creating anchoring sites that promote NPs dispersion and adhesion. The reduction mechanism in this polyol process involves the oxidation of EG to glycolate or oxalate species, which in turn donate electrons to the metal ions: Pt^{4+} and Rh^{3+} ions are reduced to Pt^0 and Rh^0, respectively. Thus, the co-reduction in Pt and Rh precursors in the presence of the functionalized carbon allows the formation of NPs on the carbon surface, without the need for additional stabilizing agents. According to ICP-OES analyses, all samples exhibited metal loadings close to 20 wt.%, which is important since our catalytic results will be compared to the commercial Pt/C electrocatalyst, which holds this metal quantity. Moreover, Pt/C is widely recognized as

a benchmark material, serving as the standard reference for evaluating the activity and stability of newly developed catalysts. The Pt:Rh ratios determined by this technique were used to designate each catalyst as $Pt_{95}Rh_5/C$, $Pt_{90}Rh_{10}/C$, $Pt_{85}Rh_{15}/C$, and $Pt_{80}Rh_{20}/C$.

The TEM images (Figure 1A–D) illustrate differences in Pt_xRh_y NPs supported on carbon Vulcan XC-72 with increasing rhodium content across the series. In all images, the carbon support displays a structure composed of aggregated carbon spheres with low contrast, over which the Pt_xRh_y NPs are dispersed as darker, high-contrast features. In Figure 1A ($Pt_{95}Rh_5/C$), the spherical-like NPs appear relatively well distributed across the support, although some regions display clustering or agglomeration. Figure 1B ($Pt_{90}Rh_{10}/C$) reveals more pronounced agglomeration. However, one can see that as the Rh content increases further, the NPs dispersion improves. In Figure 1C ($Pt_{85}Rh_{15}/C$), the NPs are more evenly distributed with reduced clustering compared to Figure 1A,B The trend continues in Figure 1D ($Pt_{80}Rh_{20}/C$), which exhibits the most homogeneous dispersion. Such a feature suggests that the increased Rh content modulates the metal nucleation process, possibly enhancing reduction homogeneity and limiting particle growth. The NPs for the higher Rh content are well dispersed across the carbon matrix, with minimal signs of agglomeration, indicating that the higher Rh content plays a critical role in stabilizing particles and promoting uniform deposition following our synthetic methodology. The $Pt_{80}Rh_{20}/C$ sample (Figure S1) was taken as a representative example for nanoparticle size evaluation, as it presents less agglomeration, yielding an average diameter of XX ± XX nm. The observation of the nanoparticle sizes was generally comparable across the different compositions; however, as previously noted, partial agglomeration was observed in certain samples, which limited the precise determination of their individual sizes in some samples.

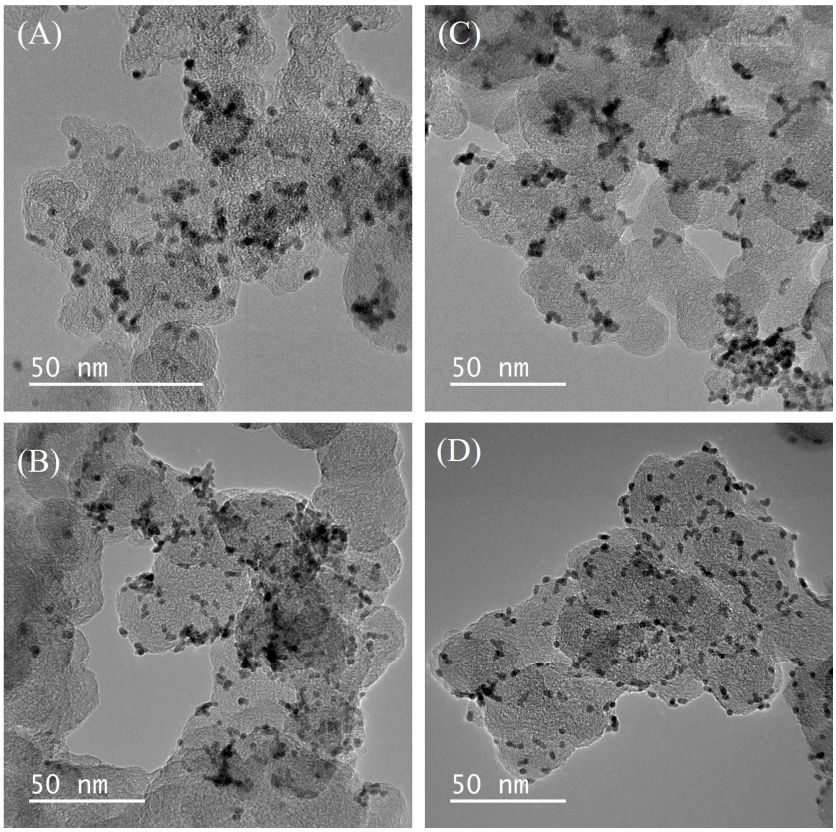

Figure 1. TEM images of Pt_xRh_y NPs supported on carbon Vulcan XC-72. (**A**) $Pt_{95}Rh_5/C$, (**B**) $Pt_{90}Rh_{10}/C$, (**C**) $Pt_{85}Rh_{15}/C$, and (**D**) $Pt_{80}Rh_{20}/C$.

The HRTEM image shows a nanoparticle deposited on the carbon support, where the darker contrast region at the center corresponds to the nanoparticle (Figure 2A). The elemental mapping images (Figure 2B–D) show that the C signal (Figure 2B) appears intense and uniformly distributed across the region, while the Pt (Figure 2C) and Rh signal (Figure 2D) are also uniformly dispersed, albeit with the latter showing a lower intensity, as expected given the low Rh content. The co-localization of Pt and Rh within the same regions, without indications of Rh-rich clusters or separate domains, strongly suggests that Rh atoms are spatially distributed in close association with Pt atoms.

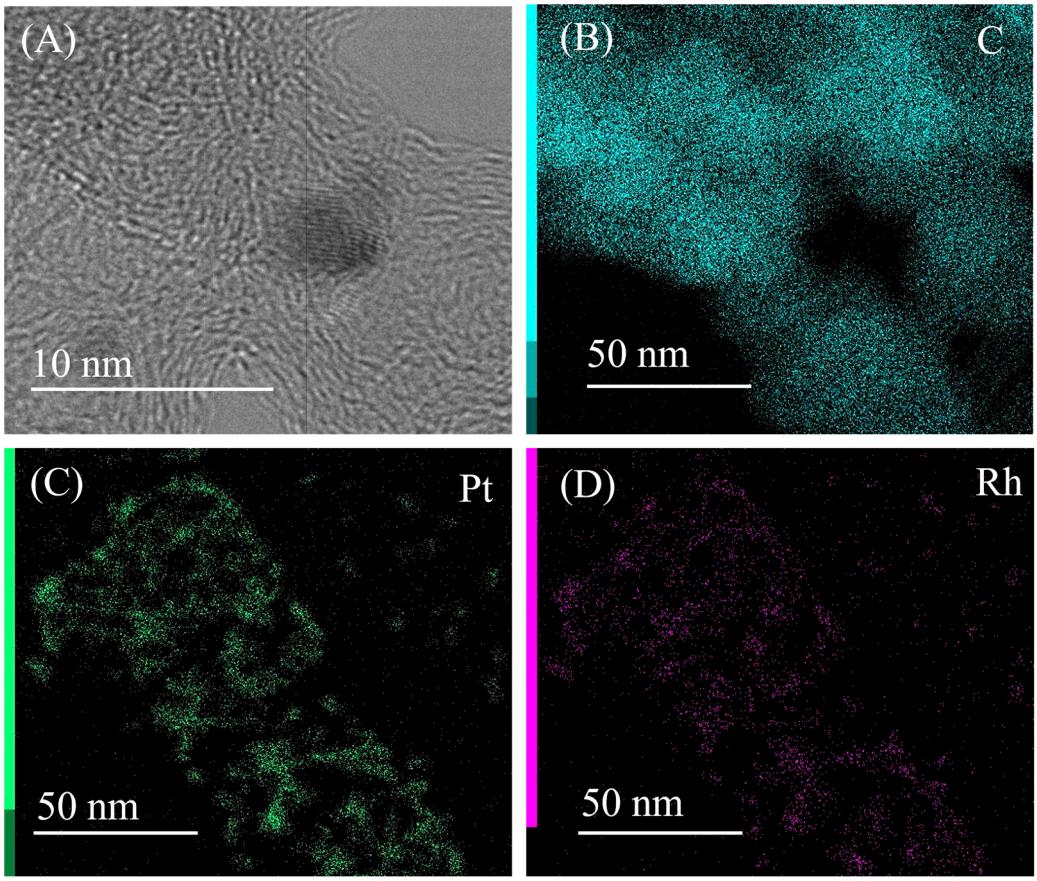

Figure 2. (**A**) HRTEM images of the $Pt_{95}Rh_5$/C electrocatalyst and elemental mapping of (**B**) C, (**C**) Pt, and (**D**) Rh.

In Figure 3, we can observe that each sample exhibits the characteristic diffraction peaks of the face-centered cubic (fcc) structure of platinum, with reflections corresponding to the (111), (200), (220), and (311) planes observed at approximately 39.8°, 46.2°, 67.4°, and 81.3° (2θ), respectively [29]. Such data was compared with the commercial Pt/C electrocatalyst. These reflections are consistent with metallic Pt and are maintained across all bimetallic samples, indicating that the fcc crystalline structure is preserved upon the incorporation of Rh. Additionally, no secondary peaks attributable to metallic Rh or rhodium oxides are detected, suggesting that there is no phase segregation. The broad peak near 25°, associated with the (002) plane of amorphous carbon, confirms the presence of the Vulcan XC-72 support [30]. Importantly, the lack of any noticeable shift in the Pt diffraction peaks with increasing Rh content indicates that no significant lattice contraction or expansion takes place, and therefore, the formation of a true Pt-Rh alloy cannot be confirmed from the XRD results. This observation is consistent with the EDS analyses, which revealed that Pt and Rh are co-localized in the same regions but not necessarily forming an alloy. Further theoretical calculations will provide additional insights into this issue.

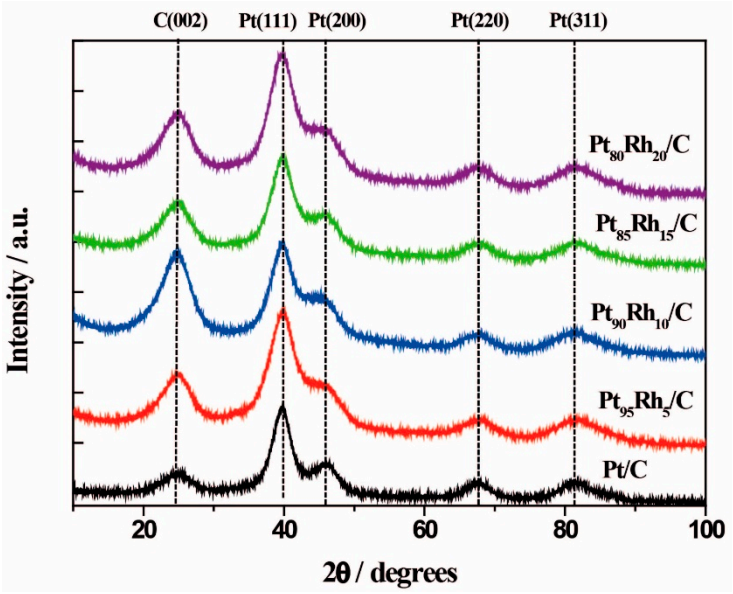

Figure 3. XRD pattern of the studied electrocatalysts.

Figure S2 shows the CO stripping peaks observed for the Pt/C and Pt_xRh_y/C electrocatalysts in 0.5 M H_2SO_4 solution in a potential window of 0.05 to 0.90 V vs. RHE. It is observed that there is no significant variation in the potential for the onset of oxidation of the adsorbed CO, occurring at approximately 0.66 V for all samples. However, the load associated with CO stripping in the catalyst $Pt_{95}Rh_5$/C is substantially higher compared to the other samples, followed by the sequence Pt/C, $Pt_{90}Rh_{10}$/C, $Pt_{80}Rh_{20}$/C, and $Pt_{85}Rh_{15}$/C. This result indicates that $Pt_{95}Rh_5$/C is more susceptible to CO adsorption, unlike the other Pt_xRh_y/C compositions, which present a relatively more resistant or tolerant behavior to CO poisoning. It can be suggested that, in catalysts with higher Rh content, the Pt-CO interaction becomes weaker, which facilitates the faster desorption of CO species from the surface and helps maintain Pt active sites available for subsequent reactions. The ECSA values, obtained through the CO stripping analysis, show that $Pt_{95}Rh_5$/C has the largest area (7.27 cm^2), followed by Pt/C (6.55 cm^2), $Pt_{90}Rh_{10}$/C (4.98 cm^2), $Pt_{85}Rh_{15}$/C (4.06 cm^2), and $Pt_{80}Rh_{20}$/C (3.96 cm^2).

Following, the electrocatalytic performances of the Pt_xRh_x/C electrocatalysts were initially performed in a 0.5 M solution of H_2SO_4 and a 0.1 M solution of KOH. The CVs of the electrocatalysts at 0.5 M $HClO_4$ and 0.1 M KOH without glycerol, both N_2-saturated, are shown in Figure 4A,B. In the potential range between −0.13 V and 0.27 V vs. RHE in acidic medium, the hydrogen adsorption and desorption processes on the surface of the electrocatalysts can be identified. In alkaline medium, these same processes are observed within the potential window of 0.74 V to 0.42 V vs. RHE. Additionally, in the acid medium, the onset of Pt and Rh surface oxide formation begins at approximately 0.78 V vs. RHE, while oxygen evolution is observed from 1.49 V vs. RHE. In alkaline medium, these processes occur at 0.50 V for oxide formation and 1.56 V vs. RHE for oxygen evolution. In the cathodic scan, the reduction in the previously formed Pt surface oxide occurs from 0.94 V vs. RHE in both acidic and alkaline media. However, in the acidic environment, as the Rh content increases, a distinct anodic peak emerges at approximately 0.5 V vs. RHE, which may be attributed to the formation of Rh oxides and hydroxides, resulting from the activation of water molecules at Rh-active sites [31–33].

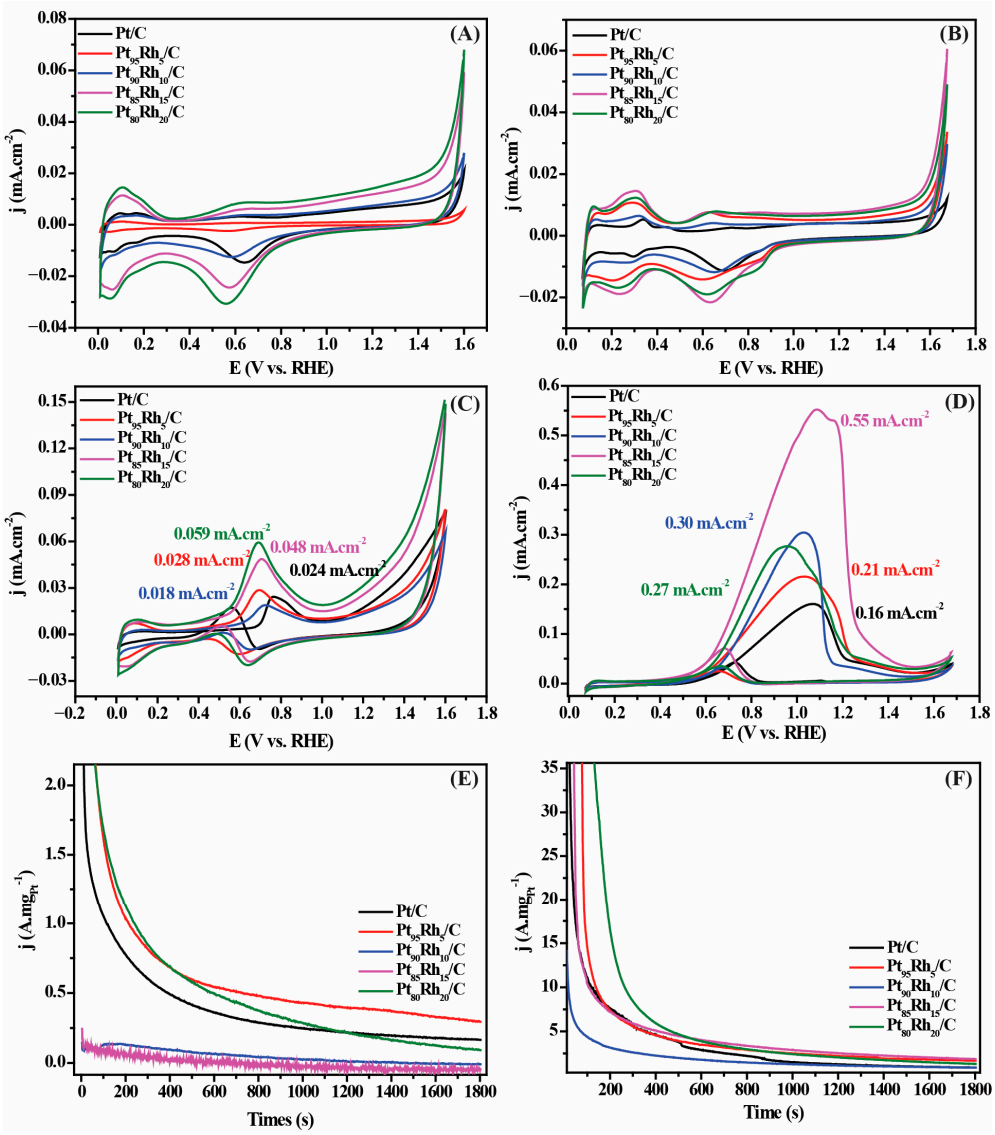

Figure 4. Electrochemical characterization of Pt_xRh_y/C electrocatalysts. (**A**,**B**) CVs recorded in N_2-saturated 0.5 M H_2SO_4 and 0.1 M KOH without glycerol. (**C**) CVs in 0.5 M H_2SO_4 + 0.1 M glycerol. (**D**) CVs in 0.1 M KOH + 0.1 M glycerol. (**E**,**F**) Chronoamperometry at 0.96 V (alkaline) and 0.69 V (acid) for 1800 s.

Figure 4C shows the CV profile of electrocatalysts prepared in $HClO_4$ 0.1 M with 0.1 M $C_3H_8O_3$. As can be seen, the addition of Rh considerably increased the current density, with the exception of $Pt_{90}Rh_{10}/C$. In addition, these catalysts not only increased their oxidation peaks, but the effect of the Pt-Rh interaction improved the electrocatalysts, shifting their potentials to around 0.3 V vs. RHE to $Pt_{80}Rh_{20}/C$, $Pt_{95}Rh_5/$, $Pt_{85}Rh_{15}/C$, and to around 0.5 V vs. RHE for $Pt_{90}Rh_{10}/C$, compared to 0.7 V vs. RHE for the Pt/C electrocatalyst. In the reverse scanning, a distinct peak appears near 0.8 V vs. RHE, associated with metal surface reactivation. This reactivation probably results from the reduction in adsorbed intermediates formed during glycerol oxidation, which temporarily block the active sites and are subsequently removed in the cathodic scan.

Figure 4D shows the CV profile of the electrocatalysts at 0.1 M KOH with 0.1 M $C_3H_8O_3$. Similarly to the acidic medium, glycerol electrooxidation occurs in the region associated with the formation of metal oxides and hydroxides, starting around 0.5 V vs. RHE. In alkaline media, however, the high concentration of OH^- ions enhances the oxidation process due to their direct involvement in the reaction mechanism and the

intrinsically higher catalytic activity of the materials under these conditions. Contrary to what was observed in the acid medium, all Pt_xRh_y/C electrocatalysts showed higher current density when compared to Pt/C, especially $Pt_{85}Rh_{15}/C$, being 2x higher than Pt/C. A cathode peak close to 0.95 V vs. RHE in the reverse scan is attributed to surface reactivation, indicating less surface poisoning compared to the acidic medium, probably due to the more efficient removal of adsorbed intermediates.

Figure 4E,F present the chronoamperometric responses recorded over 1800 s at 0.96 V vs. RHE in alkaline medium and at 0.69 V vs. RHE in acidic medium, respectively. In the acid medium, only the electrocatalyst $Pt_{95}Rh_5/C$ showed higher efficiency for glycerol electrooxidation. In alkaline medium, except $Pt_{90}Rh_{10}/C$, all electrocatalysts were more effective for glycerol oxidation, especially when compared to Pt/C. Although the current densities obtained for the samples were relatively low, possibly due to the limited regeneration of active sites during the reverse scan, the Pt_xRh_y/C catalysts proved to be more effective for glycerol oxidation. In general, they displayed higher efficiency in alkaline medium, with only one composition showing significant activity in acidic medium, likely as a result of the Pt-Rh interaction.

Durability tests were performed using CV after 30 min of electrooxidation on 0.1 M $C_3H_8O_3$ in 0.1 M electrolyte of $HClO_4$ (Figure S3A–D). The current retention values were 102.59% for $Pt_{95}Rh_5/C$, 85.77% for $Pt_{90}Rh_{10}/C$, 80.27% for $Pt_{85}Rh_{15}/C$, and 90.86% for $Pt_{80}Rh_{20}/C$. Using the 0.1 M KOH electrolyte (Figure S4A–D), the retention was 106.67% for $Pt_{95}Rh_5/C$, 78.03% for $Pt_{90}Rh_{10}/C$, 95.94% for $Pt_{85}Rh_{15}/C$, and 85.77% for $Pt_{80}Rh_{20}/C$. In the acidic medium, Pt/C exhibited a retention of 55.96% (Figure S5A), while in the alkaline medium its retention increased to 75.69% (Figure S5B). In both electrolytes, however, the Pt_xRh_y/C electrocatalysts demonstrated markedly higher retention, indicating a lower susceptibility to deactivation by adsorbed reaction intermediates. These results emphasize the existence of a trade-off between catalytic activity and long-term stability, governed by the specific Pt:Rh ratio.

Figure 5 shows the cyclic voltammetry profiles of the PtxRhy/C catalysts compared to the Pt/C in acid (0.5 M $HClO_4$) and alkaline (0.1 M KOH) media. In acid media, Pt95Rh05/C showed the highest current density (29.35 A.mgPt-1), while Pt80Rh20/C exhibited lower performance, suggesting blocking of active sites or unfavorable electronic effects. In alkaline media, the currents were significantly higher, with Pt85Rh15/C (263.81 A·mgPt-1) standing out as the most efficient composition due to a synergistic effect between Pt and Rh. In both media, Pt/C presented the lowest values, confirming that the incorporation of Rh substantially increases the electrocatalytic activity, with superior performance under alkaline conditions.

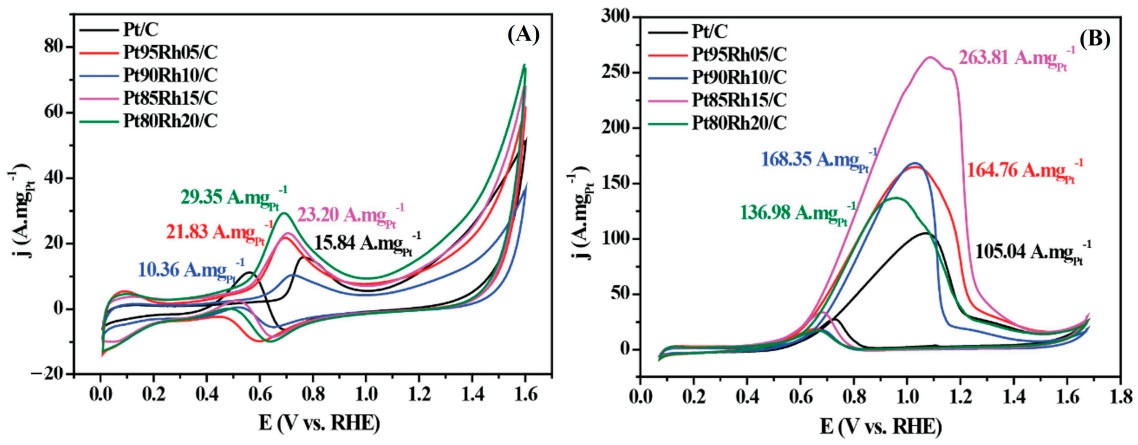

Figure 5. CV profiles of PtxRhy/C electrocatalysts as a function of Pt mass in (**A**) 0.5 M $HClO_4$ saturated with N_2 and (**B**) 0.1 M KOH at 50 mV.s^{-1}.

The results presented in Table 1 highlight the distinct stability trends among Pt-based catalysts for glycerol electrooxidation under chronoamperometric testing. The $Pt_{95}Rh_5/C$ catalyst (this work) stands out, with retention values of ≈100–105% after 1800 s in both acidic and alkaline electrolytes. By comparison, PtRu/C catalyst shows retention of ~70% under acidic conditions, reflecting its well-known bifunctional mechanism but also revealing limitations in long-term stability. The mesoporous Pt catalysts reach ~80% retention, showing that hierarchical porosity can delay deactivation relative to standard Pt/C. On the other hand, PtAu/C displayed only ~60% retention, confirming the limited stability of Au-containing systems despite improvements in onset potential and activity.

Table 1. Comparative chronoamperometric retention of Pt-based electrocatalysts for glycerol electrooxidation in acidic and alkaline media.

Catalyst	Medium	Retention over the Chronoamperometric Test Period	References
$Pt_{95}Rh_5/C$	Acidic and Alkaline	≈100–105% retention after 1800 s (acid and alkaline); no significant decay, indicating excellent stability	This work
PtRu/C	Acidic (H_2SO_4 + glycerol)	~70% retention after 1800 s; better than Pt/C (~50%) due to higher CO tolerance	[34]
PtAu/C	Alkaline (NaOH + glycerol)	~60% retention after 1800 s; better than Pt/C but limited by Au segregation	[35]
Mesoporous Pt	Alkaline (1 M NaOH + glycerol)	~80% retention after 2000 s; hierarchical porosity delays deactivation compared to Pt/C (~45%)	[36]

Thus, this comparison indicates that while compositional (PtRu, PtAu, PtRh) strategies contribute to improved durability compared to conventional Pt/C, the $Pt_{95}Rh_5/C$ catalyst surpasses these reported systems in stability under the tested conditions.

Figure 6 shows the Nyquist diagrams at a potential of 0.76 V vs. RHE in $HClO_4$ 0.1 M and at 0.87 V vs. RHE in KOH 0.1 M, which reveal the resistance to the electrooxidation process of the glycerol of the electrocatalysts. The diameter of the semicircle observed in the diagrams, when apparent, represents the charge transfer resistance (Rct) at the electrode/electrolyte interface. The smaller this diameter, the lower the Rct, thus indicating a more efficient electrical conductivity. In the acid medium, it was not possible to observe the diameter of the semicircles, probably due to the transfer resistance, and it was only possible to observe it in the alkaline medium. Except for the electrocatalyst $Pt_{90}Rh_{10}/C$, which did not present an apparent semicircle, the order of diameter for the others is $Pt_{95}Rh_5/C < Pt_{80}Rh_{20}/C < Pt_{85}Rh_{15}/C < Pt/C$.

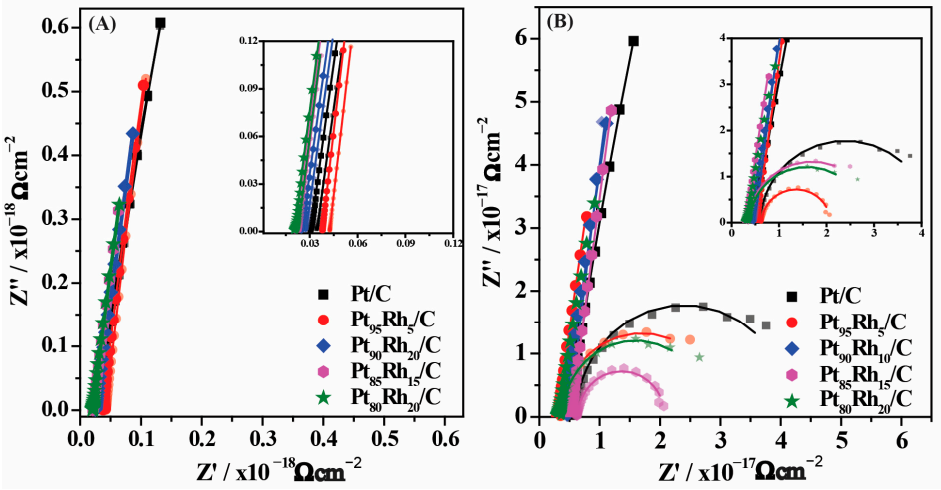

Figure 6. Nyquist diagram of the electrocatalysts in (**A**) 0.1M KOH and in (**B**) 0.1 M $HClO_4$. Electrolyte + 0.1 M glycerol. Frequency range: 1000–1 Hz.

Table 2 identifies the Rct of the electrocatalysts. These results show that the electrocatalyst with the lowest Rct was $Pt_{90}Rh_{10}/C$ in the acid medium and $Pt_{85}Rh_{15}/C$ in the alkaline medium, after the addition of $C_3H_8O_3$, which aligns well with the CV results, suggesting that $Pt_{80}Rh_{20}/C$ exhibits the lowest electron transfer resistance and the best electrical conductivity in the acidic medium, as does $Pt_{85}Rh_{15}/C$, but in the basic medium.

Table 2. EIS parameters for electrocatalysts. Electrolyte: KOH 0.1 M + glycerol 0.1 M. Frequency range: 1000–1 Hz. Potential: 0.76 V vs. RHE in $HClO_4$ 0.1 M and 0.87 V vs. RHE in KOH 0.1 M.

Electrocatalysts	No Glycerol		0.1 M $C_3H_8O_3$	
	KOH	$HClO_4$	KOH	$HClO_4$
	Rct ($\Omega.cm^{-2}$)			
Pt/C	1.90×10^5	1.54×10^5	3.54×10^3	2.19×10^5
$Pt_{95}Rh_5/C$	2.82×10^6	2.61×10^5	2.64×10^3	3.54×10^5
$Pt_{90}Rh_{10}/C$	1.66×10^6	4.89×10^6	9.91×10^5	2.38×10^6
$Pt_{85}Rh_{15}/C$	7.27×10^6	2.82×10^5	1.44×10^3	2.34×10^5
$Pt_{80}Rh_{20}/C$	3.93×10^6	3.48×10^5	2.41×10^3	1.76×10^5

A theoretical optimization of the Pt_xRh_y spherical NPs by DFTB (Figure 7) revealed that, as the Rh content increases, a limited number of Rh atoms tend to migrate toward the surface of the nanostructures. This behavior can be rationalized by considering the lower surface energy of Rh atoms compared to Pt, which favors partial surface segregation of Rh in Rh-rich systems. Furthermore, the smaller atomic radius of Rh compared to Pt leads to a confinement effect, whereby Rh atoms are more strongly retained in the inner regions of the NPs when present in low concentrations, as observed in $Pt_{95}Rh_5$. The computed binding energies for Pt_xRh_y NPs were found to be relatively similar across the series, except for the $Pt_{95}Rh_5$ composition, which exhibited a significantly different bonding energy, suggesting a less favorable alloy stabilization at very low Rh content (Table 3). Such an observation is further corroborated by the analysis of the excess energy of formation, which quantifies the relative stability of the NPs in comparison to the pure constituents. Notably, increasing Rh content results in a progressive reduction in excess energy, indicating that Rh-rich nanostructures are thermodynamically more stable and less prone to phase segregation or surface restructuring under electrochemical conditions. Therefore, the comparatively lower stability of the $Pt_{95}Rh_5/C$ catalyst, as observed in chronoamperometric measurements, can be attributed to its less favorable bonding energy and higher susceptibility to surface modification or dissolution, reinforcing the importance of the composition control in optimizing long-term electrocatalyst durability.

Table 3. Calculated binding and excess energies for Pt_xRh_y catalysts with varying Rh content.

Metal Composition	Energy (Binding)	Energy (Excess)
$Pt_{95}Rh_5$	−0.313	−6.584
$Pt_{90}Rh_{10}$	−0.308	−5.710
$Pt_{85}Rh_{15}$	−0.304	−4.806
$Pt_{80}Rh_{20}$	−0.300	−4.140

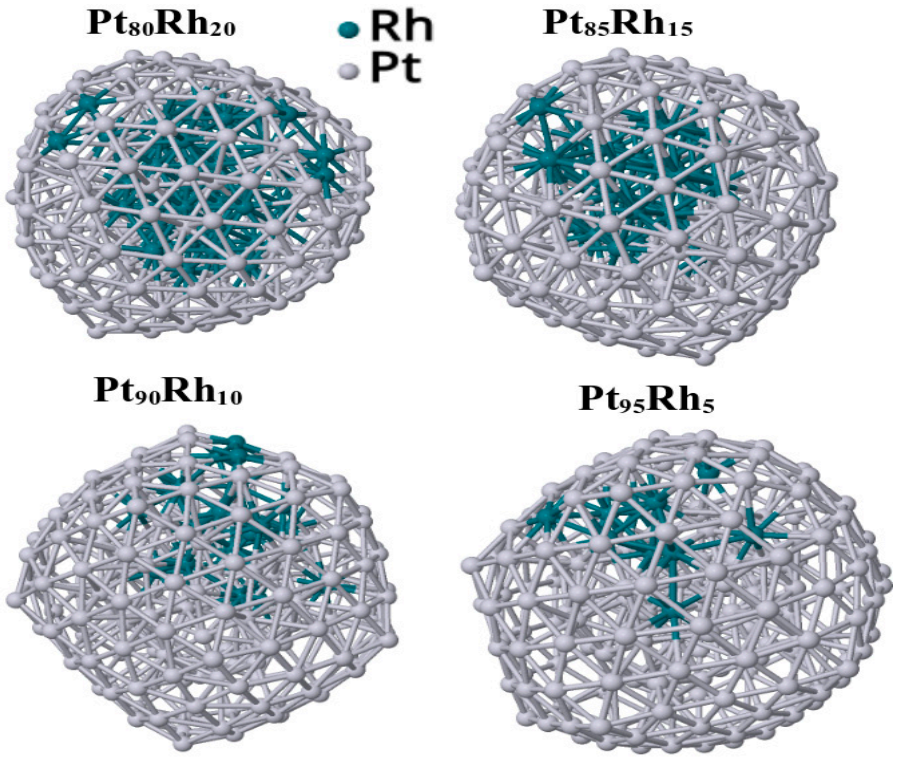

Figure 7. DFTB optimized Pt_xRh_y NPs.

4. Conclusions

This study demonstrates that the composition and atomic-scale arrangement of Pt_xRh_y bimetallic NPs significantly influence their structural, electronic, and electrochemical properties for glycerol electrooxidation. By employing a polyol-based synthesis strategy combined with pre-functionalized carbon supports, we successfully obtained a series of well-dispersed Pt_xRh_y/C electrocatalysts, as evidenced by HRTEM, EDS, and XRD analyses. Electrochemical evaluation revealed that catalytic activity is maximized in the $Pt_{95}Rh_5$/C composition.

To rationalize these observations, DFTB simulations provided insight into the energetic and structural origins of the composition-dependent behavior. The calculations indicate that Rh atoms tend to undergo partial surface segregation at higher concentrations, while remaining confined within the Pt lattice at lower levels. Importantly, $Pt_{95}Rh_5$ displays a distinct excess energy and binding energy profile compared to other compositions, consistent with its higher catalytic activity but reduced structural robustness under electrochemical stress. These findings show a trade-off between activity and stability that arises from subtle changes in the composition and atomistic configuration.

Supplementary Materials: The following supporting information can be downloaded at: https://www.mdpi.com/article/10.3390/hydrogen6040078/s1, Figure S1: Size distribution histogram prepared after measuring about 150 particles of the $Pt_{80}Rh_{20}$/C catalyst; Figure S2: CV after CO stripping voltammograms of catalysts in CO-free 0.5 M H_2SO_4 solution of the electrocatalysts. The sweep rate was 50 mV/s; Figure S3: 1st (black) and after 30 min cyclic voltammograms of glycerol oxidation (red) A) $Pt_{95}Rh_5$/C (B) $Pt_{90}Rh_{10}$/C (C) $Pt_{85}Rh_{15}$/C and (D) $Pt_{80}Rh_{20}$/C in 0.1M $HClO_4$ N_2-saturated at 50mV.s^{-1} with 0.1 M glycerol; Figure S4: 1st (black) and after 30 min cyclic voltammograms of glycerol oxidation (red) A) $Pt_{95}Rh_5$/C (B) $Pt_{90}Rh_{10}$/C (C) $Pt_{85}Rh_{15}$/C and (D) $Pt_{80}Rh_{20}$/C in 0.1M KOH N_2-saturated at 50mV.s^{-1} with 0.1 M glycerol; Figure S5: 1st (black) and after 30 min cyclic voltammograms of glycerol oxidation (red) A) Pt/C in 0.1 M $HClO_4$ and (B) Pt/C in 0.1M KOH N_2-saturated at 50mV.s^{-1} with 0.1 M glycerol.

Author Contributions: Conceptualization, R.B.d.L. and M.A.S.G.; methodology, M.V.F.R., W.D.C.d.S., L.L. and F.d.S.P.; software, A.C.A.S.; validation, R.B.d.L., E.D. and M.A.S.G.; formal analysis, R.B.d.L., E.D. and M.A.S.G.; investigation, M.V.F.R., W.D.C.d.S., L.L. and F.d.S.P.; resources, R.B.d.L. and E.D.; data curation, R.B.d.L., E.D. and M.A.S.G.; writing—original draft preparation, M.A.S.G. and F.d.S.P.; writing—review and editing, M.A.S.G., R.B.d.L. and E.D.; visualization, M.C.S.; supervision, R.B.d.L., E.D. and M.A.S.G.; project administration, R.B.d.L., E.D. and M.A.S.G. All authors have read and agreed to the published version of the manuscript.

Funding: This research received no external funding.

Data Availability Statement: The original contributions presented in this study are included in the article/Supplementary Material. Further inquiries can be directed to the corresponding author(s).

Acknowledgments: The authors gratefully acknowledge the support from Coordenação de Aperfeiçoamento de Pessoal de Nível Superior—Brazil (CAPES)—Finance Code 001 and Conselho Nacional de Desenvolvimento Científico e Tecnológico—CNPq (Marco A. S. Garcia—N○ 306151/2024-3, Eliane D'Elia—N○ 307264/2025-4). We also acknowledge the National Laboratory for Scientific Computing (LNCC/MCTI, Brazil) for providing high-performance computing resources through the SDumont supercomputer, which significantly contributed to the results reported in this work.

Conflicts of Interest: The authors declare no conflict of interest.

References

1. Soffiati, G.; Bott-Neto, J.L.; Yukuhiro, V.Y.; Pires, C.T.G.V.M.T.; Lima, C.C.; Zanata, C.R.; Birdja, Y.Y.; Koper, M.T.M.; San-Miguel, M.A.; Fernández, P.S. Electrooxidation of C_4 Polyols on Platinum Single-Crystals: A Computational and Electrochemical Study. *J. Phys. Chem. C* **2020**, *124*, 14745–14751. [CrossRef]
2. Yukuhiro, V.Y.; Gibson, A.J.; Sitta, E.; Cuesta, A.; Fernández, P.S. Effect of Cations on the Electro-Oxidation of Alcohols and Polyols on Pt: Activity, Selectivity, and Mechanistic Insights. *Curr. Opin. Electrochem.* **2025**, *52*, 101705. [CrossRef]
3. Teixeira, L.T.; de Lima, S.L.S.; Rosado, T.F.; Liu, L.; Vitorino, H.A.; dos Santos, C.C.; Mendonça, J.P.; Garcia, M.A.S.; Siqueira, R.N.C.; da Silva, A.G.M. Sustainable Cellulose Nanofibers-Mediated Synthesis of Uniform Spinel Zn-Ferrites Nanocorals for High Performances in Supercapacitors. *Int. J. Mol. Sci.* **2023**, *24*, 9169. [CrossRef] [PubMed]
4. Lima, S.L.S.; Pereira, F.S.; Lima, R.B.; Freitas, I.C.; Spadotto, J.; Connolly, B.J.; Barreto, J.; Stavale, F.; Vitorino, H.A.; Fajardo, H.V.; et al. MnO_2-Ir Nanowires: Combining Ultrasmall Nanoparticle Sizes, O-Vacancies, and Low Noble-Metal Loading with Improved Activities towards the Oxygen Reduction Reaction. *Nanomaterials* **2022**, *12*, 3039. [CrossRef]
5. Ribeiro, G.A.C.; Lima, S.L.S.; Santos, K.E.R.; Mendonça, J.P.; Macena, P.; Pessanha, E.C.; Cordeiro, T.C.; Gardener, J.; Solórzano, G.; Fonsaca, J.E.S.; et al. Zn-doped MnO_x Nanowires Displaying Plentiful Crystalline Defects and Tunable Small Cross-Sections for an Optimized Volcano-Type Performance towards Supercapacitors. *Discov. Nano* **2023**, *18*, 147. [CrossRef] [PubMed]
6. Rodrigues, M.R.M.; Ferreira, R.M.; Pereira, F.S.; Silva, F.A.; Silva, A.C.A.; Vitorino, H.A.; Júnior, J.J.G.V.; Tanaka, A.A.; Garcia, M.A.S.; Rodrigues, T.S. Application of AgPt Nanoshells in Direct Methanol Fuel Cells: Experimental and Theoretical Insights of Design Electrocatalysts over Methanol Crossover Effect. *ChemCatChem* **2022**, *14*, e202200605. [CrossRef]
7. Li, T.; Harrington, D.A. An Overview of Glycerol Electrooxidation Mechanisms on Pt, Pd and Au. *ChemSusChem* **2021**, *14*, 1472–1495. [CrossRef] [PubMed]
8. Terekhina, I.; White, J.; Cornell, A.; Johnsson, M. Electrocatalytic Oxidation of Glycerol to Value-Added Compounds on Pd Nanocrystals. *ACS Appl. Nano Mater.* **2023**, *6*, 11211–11220. [CrossRef]
9. Zhou, C.; Chen, J.; Zhao, J.; Meng, Y.; Li, Z.; Meng, X.; Wang, J. Glycerol Electrooxidation to Value-Added C_1–C_3 Chemicals: Mechanism Analyses, Influencing Factors, Catalytic Regulation, and Paired Valorization. *Renewables* **2024**, *2*, 89–110. [CrossRef]
10. Fernández, P.S.; Tereshchuk, P.; Angelucci, C.A.; Gomes, J.F.; Garcia, A.C.; Martins, C.A.; Camara, G.A.; Martins, M.E.; Da Silva, J.L.F.; Tremiliosi-Filho, G. How Do Random Superficial Defects Influence the Electro-Oxidation of Glycerol on Pt (111) Surfaces? *Phys. Chem. Chem. Phys.* **2016**, *18*, 25582–25591. [CrossRef]
11. Ye, H.; Favero, S.; Tyrrell, H.; Plub-in, K.; Hankin, A.; Rao, R.R.; Stephens, I.E.L.; Titirici, M.; Luo, H. Progress and Challenges in Electrochemical Glycerol Oxidation: The Importance of Benchmark Methods and Protocols. *ChemCatChem* **2025**, *17*, e00152. [CrossRef]
12. Zhao, Y.; Björk, E.M.; Yan, Y.; Schaaf, P.; Wang, D. Recent Progress in Transition Metal Based Catalysts and Mechanism Analysis for Alcohol Electrooxidation Reactions. *Green Chem.* **2024**, *26*, 4987–5003. [CrossRef]

13. Coutinho, J.W.D.; Figueiredo, P.B.S.; Colmati, F.; Tofanello, A.; Pereira, L.N.S.; Silva, A.C.A.; Garcia, M.A.S.; Lima, R.B. Correlating Composition and Electronic Effects of Self-Assembled PtMo Electrocatalysts for Ethylene Glycol Oxidation: An Experimental and Theoretical Approach. *Int. J. Hydrogen Energy* **2023**, *48*, 33875–33885. [CrossRef]
14. Pereira, F.S.; Santana, V.F.; Silva, A.C.A.; Tofanello, A.; Romano, P.N.; Almeida, J.M.A.R.; Rodrigues, T.S.; Rodrigues, I.A.; Lima, R.B.; Garcia, M.A.S. Electrooxidation of Ethylene Glycol Using Ag-Pt Nanotubes Supported on Silica: Correlating the Unexpected O-Vacancies Creation with Catalytic Performance. *Catal. Today* **2024**, *441*, 114914. [CrossRef]
15. Souza, M.B.C.; Soffiati, G.; Lemos, V.S.; Yukuhiro, V.Y.; San-Miguel, M.A.; Fernández, P.S. P-Block Elements Activate Pt Surfaces for the Electrooxidation of Alcohols and Polyols When Promoting the −OH Formation. *ACS Catal.* **2024**, *14*, 13105–13111. [CrossRef]
16. Garcia, M.A.S.; Ibrahim, M.; Costa, J.C.S.; Corio, P.; Gusevskaya, E.V.; Santos, E.N.; Philippot, K.; Rossi, L.M. Study of the Influence of PPh_3 Used as Capping Ligand or as Reaction Modifier for Hydroformylation Reaction Involving Rh NPs as Precatalyst. *Appl. Catal. A Gen.* **2017**, *548*, 136–142. [CrossRef]
17. Bai, J.; Mei, J.; Liao, T.; Sun, Z. Engineering Structure-Activity Relationships in Rhodium-Based Catalysts for Electrocatalysis. *Coord. Chem. Rev.* **2025**, *528*, 216418. [CrossRef]
18. Shilpa, T.; Dhanya, R.; Saranya, S.; Anilkumar, G. An Overview of Rhodium-Catalysed Multi-Component Reactions. *ChemistrySelect* **2020**, *5*, 898–915. [CrossRef]
19. Garcia, M.A.S.; Heyder, R.S.; Oliveira, K.C.B.; Costa, J.C.S.; Corio, P.; Gusevskaya, E.V.; dos Santos, E.N.; Bazito, R.C.; Rossi, L.M. Support Functionalization with a Phosphine-Containing Hyperbranched Polymer: A Strategy to Enhance Phosphine Grafting and Metal Loading in a Hydroformylation Catalyst. *ChemCatChem* **2016**, *8*, 1951–1960. [CrossRef]
20. Gupta, S.; Datta, J. A Comparative Study on Ethanol Oxidation Behavior at Pt and PtRh Electrodeposits. *J. Electroanal. Chem.* **2006**, *594*, 65–72. [CrossRef]
21. Valerio Neto, E.; Almeida, C.; Eguiluz, K.; Salazar-Banda, G. The Effect of SnO_2 and Rh on Pt Nanowire Catalysts for Ethanol Oxidation. *Catal. Res.* **2024**, *04*, 1–16. [CrossRef]
22. Lam, B.T.X.; Chiku, M.; Higuchi, E.; Inoue, H. Rhodium Nanoparticle-Loaded Carbon Black Electrocatalyst for the Glycerol Oxidation Reaction in Alkaline Medium. *Adv. Nanopart* **2016**, *5*, 60–66. [CrossRef]
23. Wang, B.; Tao, L.; Cheng, Y.; Yang, F.; Jin, Y.; Zhou, C.; Yu, H.; Yang, Y. Electrocatalytic Oxidation of Small Molecule Alcohols over Pt, Pd, and Au Catalysts: The Effect of Alcohol's Hydrogen Bond Donation Ability and Molecular Structure Properties. *Catalysts* **2019**, *9*, 387. [CrossRef]
24. Piwowar, J.; Lewera, A. On the Absence of a Beneficial Role of Rh towards C C Bond Cleavage during Low Temperature Ethanol Electrooxidation on PtRh Nanoalloys. *J. Electroanal. Chem.* **2020**, *875*, 114229. [CrossRef]
25. Coutanceau, C.; Baranton, S.; Kouamé, R.S.B. Selective Electrooxidation of Glycerol into Value-Added Chemicals: A Short Overview. *Front. Chem.* **2019**, *7*, 100. [CrossRef]
26. Kim, H.J.; Choi, S.M.; Green, S.; Tompsett, G.A.; Lee, S.H.; Huber, G.W.; Kim, W.B. Highly Active and Stable PtRuSn/C Catalyst for Electrooxidations of Ethylene Glycol and Glycerol. *Appl. Catal. B* **2011**, *101*, 366–375. [CrossRef]
27. Grimme, S.; Bannwarth, C.; Shushkov, P. A Robust and Accurate Tight-Binding Quantum Chemical Method for Structures, Vibrational Frequencies, and Noncovalent Interactions of Large Molecular Systems Parametrized for All Spd-Block Elements (Z = 1−86). *J. Chem. Theory Comput.* **2017**, *13*, 1989–2009. [CrossRef] [PubMed]
28. Bannwarth, C.; Caldeweyher, E.; Ehlert, S.; Hansen, A.; Pracht, P.; Seibert, J.; Spicher, S.; Grimme, S. Extended Tight-Binding Quantum Chemistry Methods. *Wiley Interdiscip. Rev. Comput. Mol. Sci.* **2021**, *11*, e1493. [CrossRef]
29. Cavalcante Lima, C.; Silva Fonseca, W.; Colmati, F.; Ribeiro, L.K.; Carvalho França, M.; Longo, E.; Suller Garcia, M.A.; Atsushi Tanaka, A. Enhancing the Methanol Tolerance of Ultrasmall Platinum Nanoparticles and Manganese Oxide onto Carbon for Direct Methanol Fuel Cell: The Importance of the Synthesis Procedure. *Electrochim. Acta* **2020**, *363*, 137256. [CrossRef]
30. Qin, B.; Yu, H.; Chi, J.; Jia, J.; Gao, X.; Yao, D.; Yi, B.; Shao, Z. A Novel Ir/CeO_2–C Nanoparticle Electrocatalyst for the Hydrogen Oxidation Reaction of Alkaline Anion Exchange Membrane Fuel Cells. *RSC Adv.* **2017**, *7*, 31574–31581. [CrossRef]
31. Fang, L.; Vidal-Iglesias, F.J.; Huxter, S.E.; Attard, G.A.; Wells, P.B. RhPt/Graphite Catalysts for CO Electrooxidation: Performance of Mixed Metal and Alloyed Surfaces. *Surf. Sci.* **2015**, *631*, 258–266. [CrossRef]
32. Carmargo, V.F.; Fontes, E.H.; Nandenha, J.; Souza, R.F.B.; Neto, A.O. High Activity of Pt–Rh Supported on C–ITO for Ethanol Oxidation in Alkaline Medium. *Res. Chem. Intermed.* **2020**, *46*, 1555–1570. [CrossRef]
33. Fontes, E.H.; da Silva, S.G.; Spinacé, E.V.; Neto, A.O.; de Souza, R.F.B. In Situ ATR-FTIR Studies of Ethanol Electro-Oxidation in Alkaline Medium on PtRh/C Electrocatalyst Prepared by an Alcohol Reduction Process. *Electrocatalysis* **2016**, *7*, 297–304. [CrossRef]
34. Kim, Y.; Kim, H.W.; Lee, S.; Han, J.; Lee, D.; Kim, J.; Kim, T.; Kim, C.; Jeong, S.; Chae, H.; et al. The Role of Ruthenium on Carbon-Supported PtRu Catalysts for Electrocatalytic Glycerol Oxidation under Acidic Conditions. *ChemCatChem* **2017**, *9*, 1683–1690. [CrossRef]

35. Jin, C.; Sun, C.; Dong, R.; Chen, Z. Electrocatalytic Activity of PtAu/C Catalysts for Glycerol Oxidation. *J. Nanosci. Nanotechnol.* **2012**, *12*, 324–329. [CrossRef]
36. Anil, A.; White, J.; Campos Santos, E.; Terekhina, I.; Johnsson, M.; Pettersson, L.G.M.; Cornell, A.; Salazar-Alvarez, G. Effect of Pore Mesostructure on the Electrooxidation of Glycerol on Pt Mesoporous Catalysts. *J. Mater. Chem. A Mater.* **2023**, *11*, 16570–16577. [CrossRef]